



Electrolyte Solvation Structure Design for High Voltage Zinc-Based Hybrid Batteries

Pauline Jaumaux, Shijian Wang, Shuoqing Zhao, Bing Sun* , and Guoxiu Wang* 


Zinc (Zn) metal anodes have enticed substantial curiosity for large-scale energy storage owing to inherent safety, high specific and volumetric energy capacities of Zn metal anodes. However, the aqueous electrolyte traditionally employed in Zn batteries suffers severe decomposition due to the narrow voltage stability window. Herein, we introduce N-methylformamide (NMF) as an organic solvent and modulate the solvation structure to obtain a stable organic/aqueous hybrid electrolyte for high-voltage Zn batteries. NMF is not only extremely stable against Zn metal anodes but also reduces the free water molecule availability by creating numerous hydrogen bonds, thereby accommodating high-voltage Zn||LiMn₂O₄ batteries. The introduction of NMF prevented hydrogen evolution reaction and promoted the creation of an F-rich solid electrolyte interphase, which in turn hampered dendrite growth on Zn anodes. The Zn||LiMn₂O₄ full cells delivered a high average Coulombic efficiency of 99.7% over 400 cycles.

1. Introduction

Rechargeable Zn batteries are considered as a promising technology for large-scale energy storage, owing to the inherent merits of Zn anodes, such as high specific capacity (819 mAh g⁻¹), high volumetric energy capacity (5850 mAh cm⁻³), and low redox potential (-0.76 V vs SHE). The development of Zn batteries normally focuses on the aqueous electrolyte system. However, water-based electrolytes generally engenders several shortcomings: 1) narrow electrochemical stability window (i.e., ≈2.0 V),^[1] which is dictated by hydrogen evolution reaction (HER) and oxygen evolution reaction (OER); 2) low operating voltage (e.g., about 1.44 V with MnO₂ cathode);^[2] 3) corrosion reactions to Zn anodes; and 4) dissolution of transition metal oxide in the aqueous electrolyte (e.g., the dissolution of manganese species from the widely used MnO₂ cathode material in Zn-ion batteries).^[3–7] The aforementioned drawbacks impede the development of high voltage zinc-based batteries with long cycle life. Since the potential of the electrode couples must sit

Dr. P. Jaumaux, Dr. S. Wang, Dr. S. Zhao, Dr. B. Sun, Prof. G. Wang
Centre for Clean Energy Technology, School of Mathematical and Physical Sciences, Faculty of Science, University of Technology Sydney, Ultimo NSW 2007, Australia
E-mail: bing.sun@uts.edu.au
E-mail: guoxiu.wang@uts.edu.au

Correction added on 12th August 2023, after first online publication: Ref. 14 has been updated with DOI link.

 The ORCID identification number(s) for the author(s) of this article can be found under <https://doi.org/10.1002/eam2.12578>.

DOI: 10.1002/eam2.12578

within the electrochemical stability window of the electrolytes, one major challenge to achieve high-voltage and high-energy-density Zn batteries resides in enlarging the electrochemical stability window of the electrolytes.

For this purpose, various electrolytes have been investigated via solvation structure design. For instance, “water-in-salt” electrolytes had spurred extensive research on high-voltage aqueous systems.^[8] Increasing the salt to water ratio modifies the metal cation solvation structure due to the scarce availability of free water molecules. The specific cation solvation structure, along with the restriction in the mobility of the water molecules, contributes to deferring the reduction and oxidation potential of water, thereby enlarging the electrochemical stability window of the electrolyte. This electrolyte design allowed the employment of high voltage

cathodes and prevented side reactions. Inspired by this strategy, novel electrolyte formulations emerged simultaneously, including hybrid aqueous electrolytes (e.g., “water-in-bisalt” electrolytes,^[9,10] “co-solvent-in-salt” electrolytes,^[11] eutectic solvents,^[12,13] etc.), “water-in-ionomer” electrolytes,^[14] localized highly concentrated aqueous electrolytes,^[15] and molecular crowding aqueous electrolytes.^[16]

On the other hand, organic electrolytes could be considered as an interesting alternative for high-voltage Zn batteries, owing to the wide electrochemical stability windows and super compatibility toward Zn metal without undesired corrosion reactions. However, organic solvents are also facing several drawbacks: 1) Zn salts generally show low solubility in most organic solvents; and 2) the majority of organic solvents are highly flammable, which discount the safety of the corresponding Zn battery. To date, only a few non-flammable organic systems have been reported for Zn batteries, such as phosphate-based organic electrolytes,^[17,18] hybrid aqueous/organic electrolytes,^[19,20] and hydrous organic electrolytes.^[21] However, the energy density and cycling performance of full cells still need further improvement. Therefore, further exploring promising electrolytes with large electrochemical stability windows for high-voltage Zn batteries, ensuring safety, high energy density and good cycling performances, remains a formidable challenge.

We, herein, adopt a solvation structure engineered strategy to obtain a super stable hybrid electrolyte with an electrochemical stability window of about 3.25 V for high-voltage Zn-based batteries. By introducing N-methylformamide (NMF) as an organic agent with a small amount of water, a hybrid electrolyte was prepared with the composition of 7.7 m lithium triflate (LiOTf) and 1 m zinc triflate (Zn(OTf)₂) in NMF:H₂O (the concentration is expressed in molality “m”:mol kg⁻¹_{solvent}). The solvation structure of the electrolyte was experimentally and theoretically investigated to highlight the beneficial presence of NMF in the

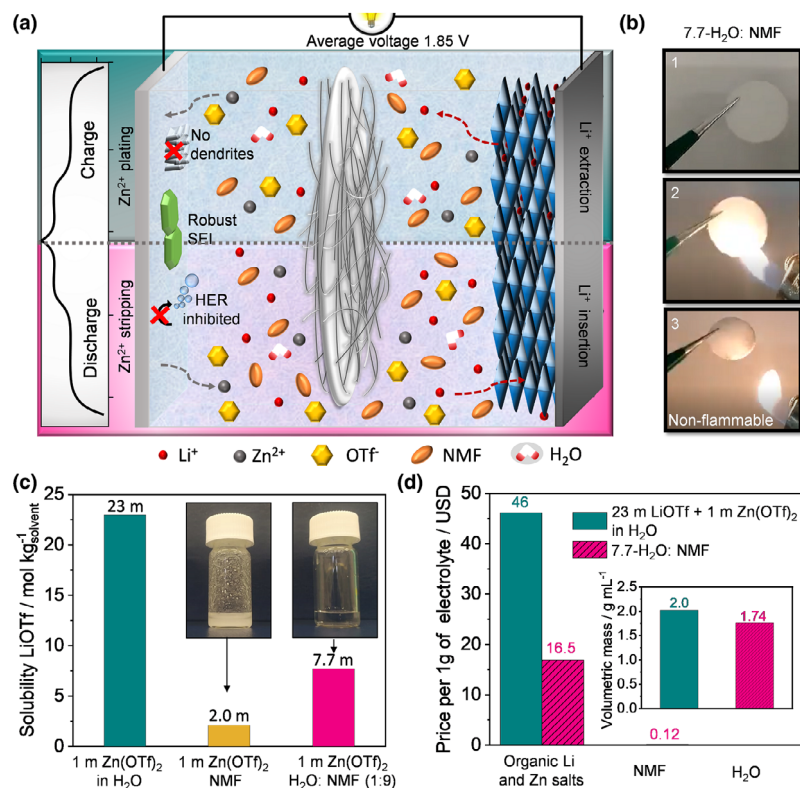


Figure 1. a) Schematic of the Zn||LMO battery system with the electrolyte of 7.7-H₂O:NMF. b) Flammability test of a glass fiber separator soaked with 7.7-H₂O:NMF electrolyte. c) Solubility limit of LiOTf in several solutions containing 1 m Zn(OTf)₂. Inset: Picture of 7.7 m LiOTf + 1 m Zn(OTf)₂ in NMF (left) and 7.7-H₂O:NMF (right). d) Price comparison between the "water-in-salt" analogue electrolyte (i.e., 23 m LiOTf + 1 m Zn(OTf)₂ in H₂O) and the 7.7-H₂O:NMF electrolyte. Inset: Volumetric mass of the 23 m LiOTf + 1 m Zn(OTf)₂ in H₂O and 7.7-H₂O:NMF.

electrolyte. NMF not only is extremely stable against Zn metal anode, but also reduces the availability of free water molecules by creating numerous hydrogen bonds and promotes the creation of a robust solid electrolyte interphase (SEI) on the Zn anode, which in turn hampered Zn dendrite growth.^[22] Meanwhile, the dissolution of transition metal elements from the cathodes into the electrolytes has been effectively suppressed. Moreover, the presence of a small amount of water is necessary to increase the solubility of LiOTf and Zn(OTf)₂ salts, and decrease the desolvation energy barrier that benefits smooth Zn plating (Figure 1a). Finally, the as-prepared electrolyte remains non-flammable owing to the presence of small amount of water molecules and the dissolved Li and Zn salts. As proof of concept, high-voltage lithium manganese oxide (LMO) cathode was coupled with Zn metal anode in the hybrid electrolyte for full cell testing. As a result, the Zn||LMO batteries were successfully cycled for more than 400 cycles with a high average voltage of 1.85 V and an excellent average Coulombic efficiency of 99.7%.

2. Results and Discussion

2.1. Formulation of the Hybrid Electrolyte

N-methylformamide is an organic solvent, which has been employed to synthesize solid-state electrolytes, but, to the best of our

knowledge, it has not been directly applied as an electrolyte solvent or additive in batteries.^[23] Amongst several organic solvents, NMF was selected owing to its high stability toward Zn anode, good miscibility with water, high polarity and high capability to form hydrogen bonds. Although NMF is flammable, this hazard is suppressed in the hybrid electrolytes (Figure 1b) owing to the low concentration of free NMF molecules (as further explained in Figure 3), which leads to reducing electrolyte evaporation (Figure S1, Supporting Information). As a result, the solvent vapor concentration in air is too lean to catch fire, thereby ensuring the safe operation of the zinc batteries. The electrolytes were prepared by dissolving 1 m Zn(OTf)₂ into a mixed solvent of NMF/H₂O. Then, a maximal amount of Li salt was introduced into the solution. The solubility limits of LiOTf in several solvents containing 1 m Zn(OTf)₂ are displayed in Figure 1c. At room temperature (25 °C), the solubility of LiOTf is about 23 m in a solution of 1 m Zn(OTf)₂ in H₂O. However, <2.5 m of LiOTf can be dissolved in the solution of 1 m Zn(OTf)₂ in NMF. When introducing a small amount of water in the mass ratio H₂O:NMF (1:9), the solubility of LiOTf increases to 7.7 m. The as-prepared 7.7 m LiOTf + 1 m Zn(OTf)₂ in H₂O:NMF electrolyte (denoted here after 7.7-H₂O:NMF) remained liquid at room temperature (inset of Figure 1c). The presence of a small amount of water not only contributes to increasing the solubility of LiOTf but also, decreases the desolvation energy barrier that benefits smooth Zn plating.^[24] Furthermore, when compared with the highly concentrated electrolyte analogue (i.e., 23 m LiOTf + 1 m Zn(OTf)₂ in H₂O), the hybrid organic/aqueous

electrolyte is also about 3-folds less expensive (Figure 1d). The 7.7-H₂O:NMF electrolyte is lighter than the analogue "water-in-salt" electrolyte (Figure 1d, inset). Therefore, for a similar battery assembly (e.g., battery case, current collector, electrodes, separator and volume of electrolyte), the batteries with the 7.7-H₂O:NMF electrolyte will present a higher energy density.

The evolution of the electrochemical stability window upon introducing the NMF solvent in the electrolyte (based on LiOTf only) was investigated by linear sweep voltammetry (LSV) analysis (Figure 2a). In Zn-ion batteries, the Zn electroplating may partially conceal the decomposition of water molecules since both reactions occur at a similar potential. Therefore, to prevent Zn plating reaction during the LSV measurement, the amount of Zn(OTf)₂ in the electrolyte was equally replaced by LiOTf. The inter-molecular interactions effectively delay the onset potentials of HER and OER, as shown in Figure 2a. Besides, the introduction of NMF significantly reduces the plateau current from -1.01 to -0.295 mA cm⁻² after introducing NMF in the mass ratio H₂O:NMF (1:9) (inset Figure 2a). When the mass percentage of NMF solvent in the electrolyte reaches 90 wt% (based on the total solvent mass), the HER is shifted to a lower potential (i.e., ≈-1.7 V vs Ag/AgCl); meanwhile, the OER occurs at a higher potential (i.e., ≈1.55 V vs Ag/AgCl) (Figure 2a). This phenomenon has been observed in highly concentrated electrolytes, where the concentration of free water molecules is dramatically

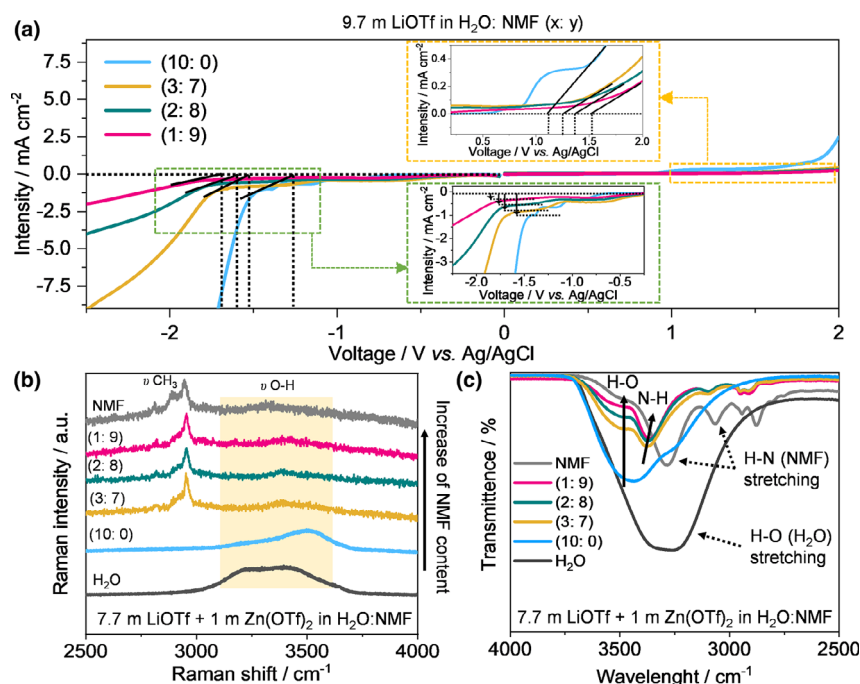


Figure 2. a) Linear sweep voltammetry spectra of 9.7 m LiOTf in H₂O:NMF with various H₂O to NMF mass ratio (H₂O:NMF mass ratio from 10:0 to 1:9). To avoid Zn deposition, 1 m Zn(OTf)₂ was replaced by 2 m LiOTf. b) Raman spectra and c) FTIR spectra of the 7.7-H₂O:NMF with various H₂O to NMF mass ratio (H₂O:NMF mass ratio of 10:0 to 1:9).

reduced. The scarce availability of free water molecules forces the creation of a unique cationic solvation shell, in which anions and/or co-solvent molecules participate.^[8,25] The electrochemical stability window of the electrolyte was widened to 3.25 V (vs 2.35 V in absence of NMF), which is largely suitable for the application of high voltage cathode LMO (as further investigated in Figure 6). Besides, the molecular crowding effect decreases the Zn plating potential to -1.35 vs Ag/AgCl (Figure S2, Supporting Information), further contributing to achieving high operational voltage of the Zn||LMO batteries.^[26] Raman spectroscopy and Fourier Transform Infra-Red (FTIR) spectroscopy were employed to elucidate the changes of the solvation structures with the increase of the NMF concentration. As seen from the Raman spectra in Figure 2b, the broad peak at $3000\text{--}3500\text{ cm}^{-1}$ is attributed to O–H stretching vibration mode of water molecules. When the concentration of the NMF solvent in the electrolyte increases, the intensity of the broad peak reduces and shifts toward lower values. These peak displacements indicate the formation of NMF–H₂O complexes through numerous hydrogen bonds between NMF and H₂O molecules.^[27,28] Accordingly, the FTIR spectra of the electrolytes confirm a decrease in the intensity of the characteristic peak of the H–O stretching of water molecules ($\approx 3300\text{ cm}^{-1}$) when the concentration of NMF increases (Figure 2c). Besides, the peaks at $\approx 3300\text{ cm}^{-1}$ corresponding to H–N stretching vibration of NMF undergo a shift toward lower wavenumbers, demonstrating the influence of NMF molecules on the solvation structure (Figure 2c). This is further verified by the bending peaks at 1650 cm^{-1} corresponding to the primary amine functional group (Figure S3, Supporting Information). Therefore, the introduction of NMF solvent inevitably contributes to reducing the free water molecules in the electrolyte. Meanwhile, NMF molecules

also create a specific cationic solvation structure, which enhances the batteries' performances.

2.2. Cationic Solvation Structure of the Hybrid Electrolyte

The Raman spectra of the electrolytes with different NMF concentrations were further investigated to characterize the cationic solvation structure (Figure 3a). The peak corresponding to the amide III functional group vibration mode at about 1250 cm^{-1} is associated with the NMF molecules.^[29] When the ratio H₂O/NMF decreases, a blue shift is observed, suggesting that NMF molecules are increasingly solvated.^[30] Therefore, NMF molecules not only closely interact with the water molecules in the electrolyte but also alter the cationic solvation shells. One of the vibrational modes of OTf[−] anions is visible at around 1040 cm^{-1} (Figure 3a). The broad peak can be deconvoluted into three peaks accordingly to the OTf solvation state, i.e., free anions, aggregate cation-anion pairs (AGG) and contact ion pair (CIP). As the concentration in NMF increases, the anionic solvation state evolves from free anions in solution to aggregate cation-anion pairs.

Molecular dynamic (MD) simulations were employed to theoretically investigate the solvation sheath of Zn and Li ions in the electrolytes. Figure 3b displays the screenshots of the molecular arrangement in the 7.7-H₂O and 7.7-H₂O:NMF electrolytes after 20 ns at 298 K. It is obvious that free water molecules are present in the 7.7-H₂O electrolyte, whereas the water molecules in the 7.7-H₂O:NMF electrolyte are surrounded and interact with NMF molecules, demonstrating efficient solvation modulating effect of NMF.^[16,31] It was recently demonstrated that in hybrid electrolytes (i.e., mixture of Li salts and Zn salts) the Zn solvation structure was unchanged when Li concentration increased.^[32] However, the addition of strong polar solvents in the aqueous electrolyte perturbs the solvation sheath of Zn²⁺ cations.^[33] The highly polar molecules can break the water clusters and preferentially solvate Zn²⁺. Therefore, the introduction of NMF molecules totally changed both Li and Zn solvation sheaths. The schematic evolution of the Zn²⁺ solvation sheath is displayed in Figure 2b. When NMF molecules are present in the electrolyte, Zn²⁺ mostly interacts with OTf[−] anions and NMF molecules, which clearly demonstrates the unique molecular arrangement due to the polar NMF molecules. Furthermore, as shown by the radial distribution function (Figure 3c,d), Zn²⁺ is preferentially coordinated with water molecules in the 7.7-H₂O electrolyte ($\text{Zn-O}_{\text{H}_2\text{O}} > \text{Zn-O}_{\text{OTf}}$). On the contrary, in the 7.7-H₂O:NMF electrolyte, Zn²⁺ cations are favorably coordinated with OTf[−] anions as fewer water molecules participate in the solvation sheath.^[34] Similarly, when NMF molecules are present in the electrolyte, OTf[−] anions enter Li⁺ solvation sheath (Figure S4, Supporting Information). Additionally, NMF molecules create additional hydrogen bonds with water molecules, which further restrict the amount of free water molecules and contribute to expand the electrochemical stability window of the 7.7-H₂O:NMF electrolyte (Figure 3e).^[28]

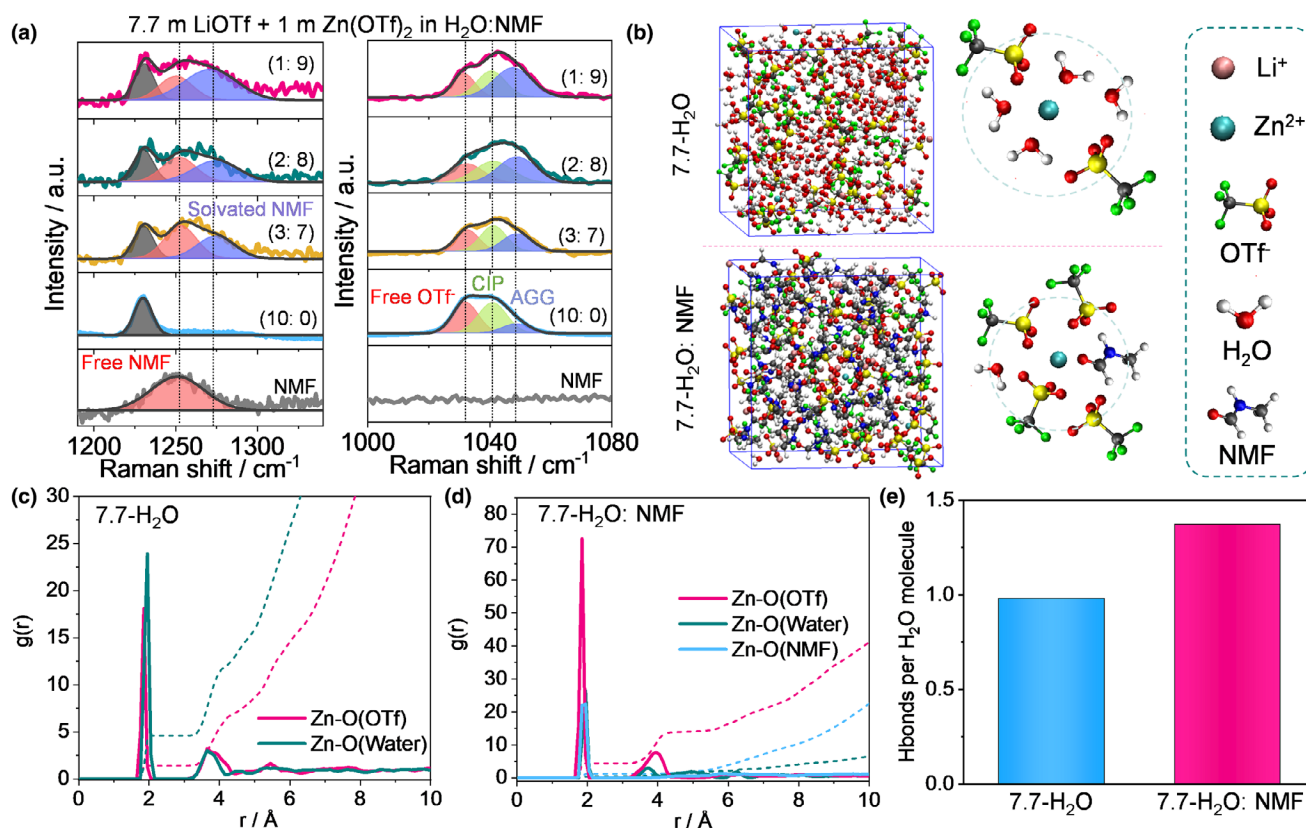


Figure 3. a) Raman spectra of pure NMF solvent and several 7.7 m LiOTf + 1 m Zn(OTf)₂ in H₂O:NMF electrolytes with variable H₂O/NMF ratios (from 10:0 to 1:9). b) Snapshots of the simulated cells with 7.7-H₂O and 7.7-H₂O:NMF after 20 ns at 298 K obtained with MD simulations and schematic representation of the solvation sheath of Zn cation in the corresponding electrolyte. The radial distribution function $g(r)$ of Zn–O(OTf), Zn–O(H₂O) and Zn–O(NMF) pairs calculated from MD simulation trajectories in c) 7.7-H₂O and d) 7.7-H₂O:NMF. e) Number of hydrogen bonds formed in 7.7-H₂O and 7.7-H₂O:NMF systems at 20 ns.

2.3. Electrochemical Performance of the Zn||LMO Full Cells

The electrochemical performances of the 7.7-H₂O:NMF electrolyte were evaluated in Zn||LMO full cells between 1.0 and 2.1 V (Figure 4; Figure S5, Supporting Information). When the 7.7-H₂O electrolyte was employed, the Zn||LMO cells exhibited a high specific capacity of 108 mAh g⁻¹ during the first 50 cycles at 1 C. However, the specific capacity severely decreased after 60 cycles and dropped to only 10 mAh g⁻¹ after 300 cycles (Figure 4a). As shown in the charge–discharge voltage profiles (Figure 4b), the cells with 7.7-H₂O electrolyte started decomposing at 2.06 V mostly due to OER, causing the drying of the cells and the decline in cycling performance.^[35] In sharp contrast, upon introducing NMF in the electrolyte, the cells with 7.7-H₂O:NMF electrolyte still delivered a capacity of 82 mAh g⁻¹ after 400 cycles, corresponding to a capacity retention of 82.3%. Meanwhile, a high Coulombic efficiency of 99.7% was achieved, attesting to the excellent cycling stability.

Additionally, the cells demonstrated no electrolyte decomposition even at a low current density of 0.1 C (Figure 4c). The rate performances of Zn||LMO cells with the electrolytes of 7.7-H₂O and 7.7-H₂O:NMF are shown in Figure 4d. A cut-off time was set equal to the theoretical charging time to prevent continuous water decomposition in the 7.7-H₂O electrolyte (i.e., cut-off time = 10 h, when the current density is 0.1 C). Both cells successfully cycled for 10 cycles at 0.1 C, delivering a specific capacity of about 110 mAh g⁻¹. However, it is

obvious that the cells with 7.7-H₂O electrolyte suffered from substantial side reactions as demonstrated by the low Coulombic efficiency of 70% (vs 96% for the cells with 7.7-H₂O:NMF at 0.1 C). As the cycling rate increased, the specific capacity obtained with the cells containing the 7.7-H₂O electrolyte dropped sharply to almost 0 mAh g⁻¹ at 1 C, due to the dried separator and the high impedance of the cells.^[32,36] As a comparison, the 7.7-H₂O:NMF electrolyte enabled the batteries to deliver a stable specific capacity even at the high rate of 5 C with a Coulombic efficiency close to 100%. When the current density was reversed back to 0.1 C, the capacity retention of the Zn||LMO cells reached 96.2% of the specific capacity at 0.1 C.^[36] Furthermore, pouch cells assembled with the 7.7-H₂O:NMF electrolyte achieved more than 200 cycles with a high average Coulombic efficiency of 99.3% (Figure S6, Supporting Information).

The impedance of Zn||LMO batteries was measured with electrochemical impedance spectroscopy (EIS) analyses driven before cycling, after 15 cycles, and after 100 cycles (Figure S7, Supporting Information). The simulation results obtained via an equivalent circuit are organized in Figure 4e and Table S1, Supporting Information. When the 7.7-H₂O electrolyte was employed, the interface resistance (R_f) and the charge transfer resistance (R_{ct}) sharply decreased between 0 and 15 cycles and then remarkably increased after 100 cycles. This phenomenon can be interpreted as an improvement in the interfacial contact reducing the impedance of the cell in the first few cycles, followed by a decline of the electrolyte amount in the cell caused by the endless water decomposition

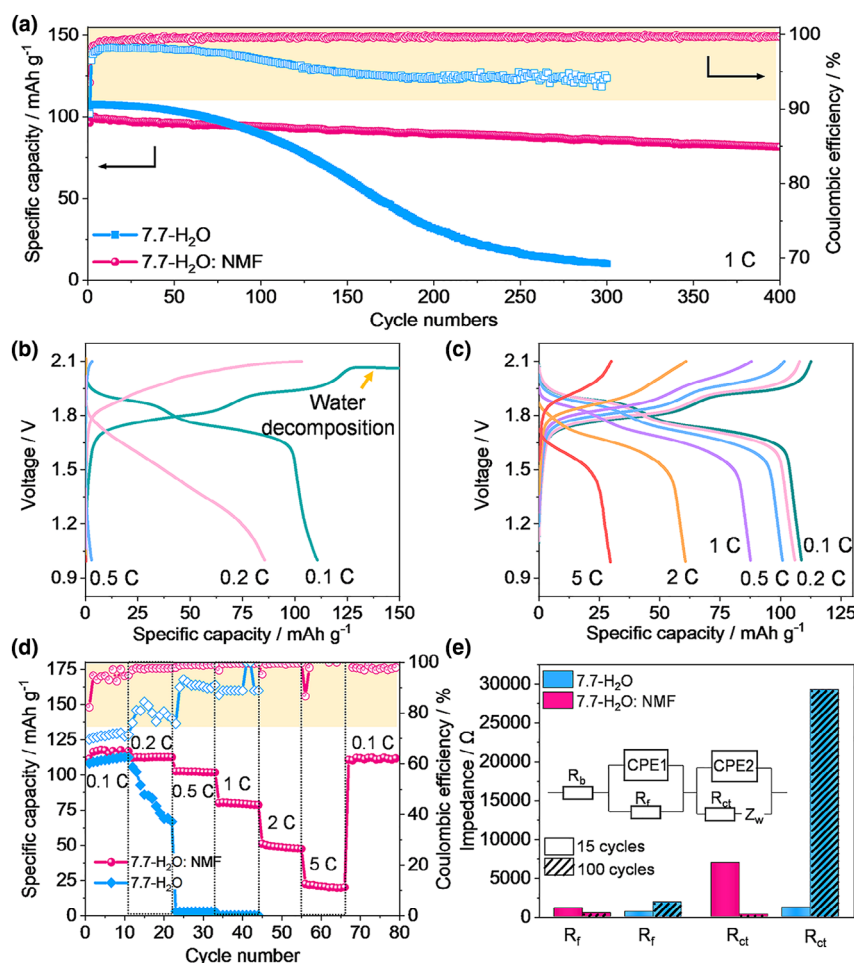


Figure 4. a) Cycling performance of Zn||LMO full cells with 7.7-H₂O (blue line) and 7.7-H₂O:NMF (pink line) electrolytes at 1 C. Charge and discharge curves of b) Zn||7.7-H₂O||LMO batteries and c) Zn||7.7-H₂O:NMF||LMO batteries at various rate from 0.1 C to 5 C and, d) corresponding rate performance of Zn||LMO full cells with 7.7-H₂O (blue diamonds) and 7.7-H₂O:NMF (pink circles) electrolytes. e) The evolution of interfacial resistance of Zn||LMO batteries with 7.7-H₂O (blue) and 7.7-H₂O:NMF (pink) electrolytes at 15 and 100 cycles.

at the electrodes, thereby leading to the drying of the cell. For comparison, after adding NMF solvent into the electrolyte, the values of R_f and R_{ct} continuously decreased from 9891 to 443 Ω , and from 11 087 to 296 Ω , respectively. The much smaller and sharply decreasing R_f in the first 15 cycles may correspond to the formation of a stable SEI that hinders continuous side reactions, while the steady diminishing R_{ct} value confirms the excellent stability of the electrolyte.^[37,38]

To further demonstrate the excellent cycling of the Zn||7.7-H₂O:NMF||LMO batteries, the electrochemical performances of several electrolyte compositions were investigated. First, Zn||LMO batteries containing 7.7 m LiOTf and 1 m Zn(OTf)₂ with various H₂O:NMF mass ratios were cycled at 1 C (Figure S8, Supporting Information). As the concentration of NMF increases in the electrolyte, the overall performance of the battery increases. The electrolyte with H₂O:NMF ratio equal to 1:9 demonstrated the highest capacity retention and excellent Coulombic efficiency. Second, several batteries were assembled with different concentrations in LiOTf (1, 3 and 7.7 m) while maintaining the Zn salt concentration to 1 m Zn(OTf)₂ and the H₂O:NMF mass ratio equal to 1:9 (Figure S9, Supporting Information). When the electrolyte of 1 m

LiOTf + 1 m Zn(OTf)₂ in H₂O:NMF was employed, the cells exhibited extremely poor cycling stability. However, by increasing the LiOTf concentration to 3 m, the capacity retention was substantially enhanced. Meanwhile, the cells with 7.7-H₂O:NMF electrolyte displayed the highest reversibility. The poorer cycling performance of the non-optimized batteries could be due to degradation of the electrolyte at high voltage caused by the narrow electrochemical stability window of these electrolytes, and poor reversibility of the Zn plating and stripping. Finally, the “water-in-salt” analogue electrolyte (i.e., 23 m LiOTf + 1 m Zn(OTf)₂ in H₂O), where NMF molecules are absent, was compared to the 7.7-H₂O:NMF electrolyte to highlight the benefits of NMF agent (Figure S10, Supporting Information). Although the Zn||LMO batteries initially cycled well in the “water-in-salt” electrolyte, the capacity considerably degraded after 250 cycles, attesting of the underlying side reactions occurring in the battery. We suggest that the “water-in-salt” electrolyte cannot totally prevent HER and OER at high voltage, as suggested by the narrower electrochemical stability window (Figure S10a, Supporting Information). The small amount of water degradation occurring at each cycle could lead to the crystallization of the electrolyte and the sharp capacity fading after 250 cycles (Figure S10b, Supporting Information). These observations suggest that the synergistic contribution of LiOTf salt concentration and NMF modulator agent are essential to obtain optimal electrochemical performances.

2.4. Characterization of Zinc Anodes

The compatibility of Zn anodes with different aqueous electrolytes was observed by field-emission scanning electron microscope (FE-SEM) (Figure S11, Supporting Information). The Zn metal foils were submerged in 7.7-H₂O and 7.7-H₂O:NMF electrolytes, and in H₂O and NMF pure solvents for several days. After being immersed for 49 days in pure H₂O, the Zn metal foil displayed crystalline spear-shaped morphologies. Although less obvious, similar morphologies were observed on the Zn foil that was submerged in the electrolyte of 7.7-H₂O. As verified with XRD, the white crystalline deposit corresponds to zinc hydroxide (Zn(OH)₂) and zinc oxide (ZnO) species (Figure S12, Supporting Information). The byproducts were formed from the parasitic reactions between water molecules and Zn metal due to the more alkaline nature of these two solutions (Figure S13, Supporting Information).^[39,40] In contrast, the Zn foils remained uncorroded in pure NMF solvent and the 7.7-H₂O:NMF electrolyte, attesting to the remarkable compatibility of the as-prepared electrolyte with Zn metal.

The reversibility of Zn plating and stripping was investigated in Zn symmetric cells at different current densities ranging from 0.1 to 2 mA cm⁻², with a cut-off capacity of 0.1 to 2 mAh cm⁻². As shown

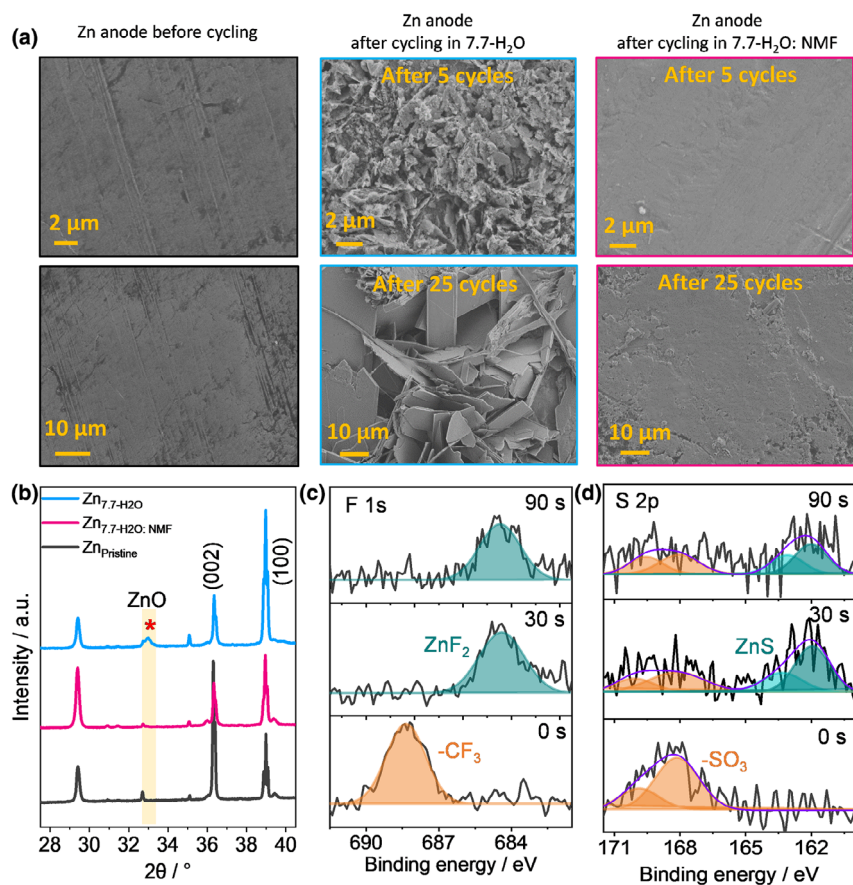


Figure 5. a) FE-SEM images of the pristine Zn anode, and Zn anode after 5 and 25 cycles in 7.7-H₂O and 7.7-H₂O:NMF. b) The corresponding XRD profiles of the Zn anode after 25 cycles in different electrolytes. The c) F 1s, d) S 2p XPS depth profiling spectra of the Zn anode retrieved from Zn||LMO batteries after 25 cycles with 7.7-H₂O:NMF electrolytes.

in Figure S14, Supporting Information, the overpotential remained constant for each current density, attesting to the reversible Zn plating and stripping processes. However, the Zn symmetric cells in the absence of NMF suffered from soft short-circuit at a current density of 0.5 mA cm⁻² and the cells short-circuit when the current density reached 2 mA cm⁻². The Coulombic efficiency of the Zn plating and stripping processes was evaluated in half-cells (Figure S15, Supporting Information). The half-cells with the 7.7-H₂O:NMF electrolyte delivered a high average Coulombic efficiency of 98.2% over 100 cycles and 98.5% over 300 cycles, demonstrating the superior reversibility of the Zn chemistry in the 7.7-H₂O:NMF electrolyte. In contrast, the half-cells with the 7.7-H₂O electrolyte exhibited an average Coulombic efficiency of 94.3% over 100 cycles. To further characterize the Zn deposition process, the Zn deposition obtained by plating 1.5 mA h cm⁻² Zn on Cu substrate at 0.1 mA cm⁻² was observed with FE-SEM images (Figure S16, Supporting Information). The Zn plating appears smoother and denser when NMF is present in the electrolyte. Furthermore, when using the 7.7-H₂O:NMF electrolyte, the nucleation potential was drastically reduced from 447.7 to 51.6 mV (Figure S17, Supporting Information). This suggests that during the Zn deposition, the Zn ions must overcome a smaller energy barrier.^[41] Therefore, numerous Zn nuclei can form on the surface of the Zn anode, thereby facilitating a uniform plating. In order to attest the dendrite growth in full cell systems, the

cycled Zn anodes were retrieved from Zn||LMO full cells after 5 and 25 cycles in different electrolytes, and the morphologies were analyzed by FE-SEM (Figure 5a). The Zn anode cycled in the 7.7-H₂O electrolyte presented sharp dendrites after only 5 cycles. In comparison, the morphology of the Zn anode that had cycled in the 7.7-H₂O:NMF electrolyte remained smooth without apparent dendrite growth after 25 cycles. The suppression of dendrites can be attributed to several factors, such as the decrease of the Zn²⁺ ion desolvation energy owing to the high ion concentration in the electrolyte and the more acidic pH value of the electrolyte (Figure S13, Supporting Information).^[24,42] Furthermore, the XRD spectrum of the Zn anode, which had cycled for 25 cycles in the electrolyte of 7.7-H₂O, displayed an obvious peak at 33° corresponding to ZnO species. In contrast, this peak vanished when NMF was present in the electrolyte (Figure 5b). XPS depth profiling analyses further confirmed the absence of ZnO species on cycled Zn electrode (Zn 2p, peak ≈1022.3 eV) suggesting that the reactivity of H₂O molecules is dramatically limited (Figure S18a, Supporting Information).^[43,44] The F 1s, S 2p and C 1s spectra clearly exhibited peaks corresponding to inorganic and organic compounds (Figure 5c,d; Figure S18b, Supporting Information).^[45,46] The substantial amount of ZnF₂ and ZnS species suggests an anion-driven SEI layer formation mechanism. To further investigate the SEI formation mechanism, the lowest unoccupied molecular orbital (LUMO) energy levels of each ion-solvent complex were calculated (Figure S19, Supporting Information). Upon the introduction of NMF in the electrolyte, the LUMO energy levels of the Li and Zn solvation complexes dramatically decreased. This suggests that the formation of an SEI deriving from the decomposition of these complexes has been facilitated in the 7.7-H₂O:NMF electrolyte.^[47]

2.5. Investigation on the LMO Cathodes

The electrochemical mechanism occurring at the cathode side was investigated to deepen our understanding of the Zn||LMO hybrid systems with 7.7-H₂O:NMF electrolyte. The cyclic voltammograms (CVs) of LMO cathodes in the electrolyte with and without NMF exhibit two conventional oxidation peaks at ≈1.8 and ≈2.0 V versus Zn/Zn²⁺ and two reduction peaks at ≈1.7 and ≈1.9 V versus Zn/Zn²⁺, corresponding to the intercalation and deintercalation of Li⁺ ions, respectively (Figure 6a).^[48] As observed, there is a noticeable peak shift in the CV curves after adding NMF in the electrolyte. According to the Nernst equation (Equation 1), the Li potential insertion is influenced by the Li chemical activity. The introduction of NMF affects the Li solvation sheath, which results in an upward shift in the Li insertion potential in LMO cathode. This phenomenon has been observed in previous works on highly concentrated electrolytes.^[13]

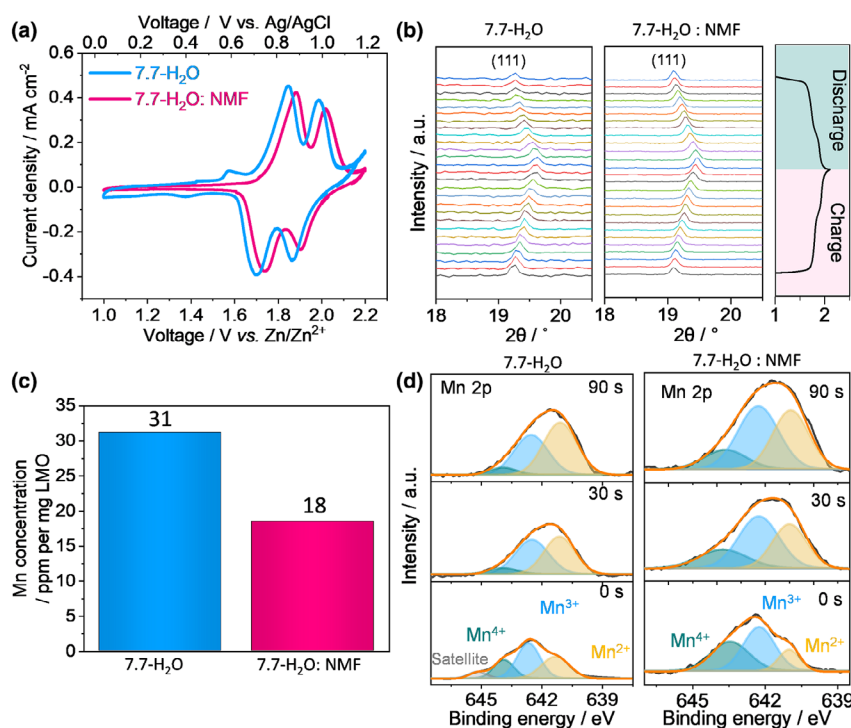


Figure 6. a) Cyclic voltammograms of the LMO cathodes in the electrolytes of 7.7-H₂O (blue line) and 7.7-H₂O:NMF (pink line) at 1 mV s⁻¹. b) In-situ XRD spectra of the LMO cathodes during the 5th cycle in the electrolytes of 7.7-H₂O (left) and 7.7-H₂O:NMF (right) at 0.2 C. c) The amounts Mn species on the separators after 25 cycles in the electrolytes without NMF (blue) and with NMF (pink), obtained with ICP-MS analysis. d) XPS depth profiling presenting the Mn 2p_{3/2} spectra of LMO cathodes after 25 cycles in the electrolytes without NMF (left) and with NMF (right).

$$E_{\text{Red}} = E_{\text{Red}}^0 - \frac{RT}{zF} \ln \left(\frac{a_{\text{Red}}}{a_{\text{Ox}}} \right) \quad (1)$$

where E is the half-cell reduction potential, E^0 is the standard half-cell reduction potential, R is the universal gas constant, T is the temperature, z is the number of electrons transferred in the half-cell reaction, F is the Faraday constant, and a is the chemical activity (Red and Ox corresponds to the reduced and oxidized form, respectively). In-situ XRD was employed to further investigate the Li⁺-ion intercalation and deintercalation behaviors during cycling. Figure 6b displays the in-situ XRD spectra of the 5th cycle in the Zn||LMO full cell with and without NMF at 0.2 C. During the charge process, there is an obvious shift toward higher angle of the (111) peak, attesting to the extraction of Li⁺-ions, whereas during the discharge process, the peak shifts back to its original position, confirming the reversible Li ions insertion and extraction. The CV and in-situ XRD spectra further demonstrate that Zn²⁺ ions do not intercalate in LMO cathode.^[49] One of the major drawbacks of spinel LMO cathodes is the capacity fading caused by the disproportionation of trivalent manganese (Mn³⁺) into divalent and tetravalent manganese (i.e., Mn²⁺, Mn⁴⁺) species. Mn²⁺ is highly soluble in aqueous electrolytes, which engenders irreversible crystallographic structural changes and dramatic capacity fading.^[50,51] After 25 cycles, the separators were retrieved from the cells with 7.7-H₂O and 7.7-H₂O:NMF electrolytes and analyzed by inductively coupled plasma mass spectroscopy (ICP-MS) in order to quantify the Mn²⁺ species present in the electrolytes (Figure 6c).

The amount of Mn²⁺ compounds in the 7.7-H₂O electrolyte was close to two-fold higher than that with the 7.7-H₂O:NMF electrolyte, signifying that the presence of the NMF molecules significantly impedes the dissolution of Mn species from the cathode into the electrolyte. Furthermore, LMO cathodes were analyzed by XPS depth profiling, which confirmed the excess of Mn²⁺ species soluble in the 7.7-H₂O electrolyte (Figure 6d, left). As a comparison, the XPS depth profiling spectra displayed a large amount of Mn³⁺ species as well as reduced Mn²⁺ species in the LMO cathode which cycled in the 7.7-H₂O:NMF (Figure 6d, right). The inter-molecular interaction between NMF and water molecules largely obstructs the disproportionation of Mn³⁺ and the Mn²⁺ dissolution in the electrolyte, thereby resulting in high cycling performance of the Zn||7.7-H₂O:NMF||LMO full cells.

3. Conclusion

The electrolyte solvation structure was carefully modified by introducing NMF into an aqueous electrolyte composed of 7.7 m LiOTf, 1 m Zn(OTf)₂ and water. We found that the NMF molecules closely interact with water molecules and disturb the Zn²⁺ cation sheath structure. The diverse benefits resulting from inter-molecular interactions include: 1) the electrochemical stability window was dramatically extended, allowing the successful application of electrodes with high voltage redox couples such as the LMO cathode; 2) the zinc plating and stripping processes were improved owing to the lower Zn desolvation energy barrier; 3) a robust inorganic-rich SEI was formed on the Zn anode, which prevented Zn dendrite growth; and 4) the transition metal dissolution from the LMO cathode into the electrolyte was reduced due to the small amount of free water molecules in the crowded electrolyte. Furthermore, the as-prepared electrolyte is non-flammable and less expensive than “water-in-salt” analogues. Moreover, Zn||LMO full cells with the solvation engineered structure electrolyte exhibited excellent cycling stability and high average Coulombic efficiencies in both coin cells and pouch cells, indicating their promising potential for practical applications. Besides, this electrolyte design could also be adapted to other high voltage cathode materials in sodium and potassium energy storage systems.

4. Experimental Section

Electrolyte preparation: Zinc trifluoromethanesulfonate (Zn(OTf)₂, 98%; Sigma Aldrich) and lithium trifluoromethanesulfonate (LiOTf, 99.995% trace metals basis; Sigma Aldrich) salts, and NMF (99%; Sigma Aldrich) solvent were used as received without further purification. The electrolytes were simply prepared by dissolving 1 m of Zn(OTf)₂ in water and then, adding a certain amount of LiOTf salt at 40 °C, where the unit “m” is molality (i.e., mole of salts per kilo of solvent) and “M” correspond to molarity (i.e., mole of salts per liter of solvent).

Electrolyte characterizations: The electrochemical stability window of the electrolytes was measured via linear sweep voltammetry (LSV) method using the

VMP3 (Bio Logic Science Instruments) multichannel electrochemical station. In order to observe HER and OER potential, the zinc species in the electrolyte were replaced by lithium species, and the anion mole number was conserved (i.e., 1 m Zn(OTf)₂ was replaced with 2 m LiOTf). In this case, the testing cell was a three-electrode system with titanium foil as working electrode, platinum wire as counter electrode and a silver/silver chloride reference electrode. The voltage range was from the open circuit voltage (OCV) to 2.0 V versus Ag/AgCl for the positive scan and from the OCV to -2.5 V versus Ag/AgCl for the negative scan at the scan rate of 10 mV s⁻¹. The electrochemical stability window of the electrolyte containing Zn salts was also measured in a two-electrodes system with Zn foil as the counter and reference electrode and stainless-steel blocking electrode as the working electrode. The voltage range was from the open circuit voltage (OCV) to 3.0 V versus Zn/Zn²⁺ for the positive scan and from the OCV to -2.0 V versus Zn/Zn²⁺ for the negative scan at the scan rate of 10 mV s⁻¹. The Fourier transform infrared (FT-IR) spectra of the electrolytes were obtained with a Nicolet Magna 6700 spectrometer at room temperature. The Raman analyses were effectuated with a Renishaw Raman spectrometer system (Gloucestershire, UK). For the combustion test, 100 µL of electrolyte sample was dropped onto a glass fiber separator and exposed to a flame for 5 s. The mass retention of different electrolyte samples was measured by aging at room temperature under atmospheric condition.

The static stability of the electrolyte toward Zn metal anode was qualitatively observed by introducing a piece of Zn metal into different electrolytes. After 49 days, SEM observations (Zeiss Supra 55VP) and XRD (Bruker D8 discover) measurements were effectuated.

Electrochemical performances: The electrochemical performances were evaluated in coin cells (mass of the casing including spacer and spring ≈2.5 g; mass of the separator ≈13.6 mg and mass of electrodes ≈50 mg). The half cells were assembled with Zn and Cu electrodes. The electrolyte was dropped on a GF separator. The cells were aged for 6 h and then cycled at 0.1 mA cm⁻² at 0.1 mAh cm⁻², with a 1 V cut off voltage. The symmetric cells were assembled with two Zn electrodes, and GF separator. The cells were also aged for 6 h before cycling at a different current density.

Lithium manganese oxide (LiMn₂O₄, LMO) was purchased from Shanshan Co., Ltd. The cathodes were prepared by mixing the active material with carbon black and polyvinylidene fluoride (PVDF; Sigma Aldrich) binder with a mass ratio of 80:10:10 in anhydrous *N*-methyl-2-pyrrolidone (NMP; Sigma-Aldrich). The obtained slurry was coated onto a Ti foil current collector and dried in a vacuum oven overnight at 70 °C. The CVs of LMO electrodes were recorded in a two-electrode system with Zn foil as the counter and reference electrode at 1 mV s⁻¹. The Zn||LMO aqueous full cells were assembled in coin cells and pouch cells with Zn foil as the anode, LMO as the cathode with a mass loading of ≈2 mg cm⁻², and glass fiber membrane (Whatman GF/A) as the separator. The electrolyte: LMO ratio in each cell was set at ≈50 µL mg⁻¹ uniformly. The electrochemical performances were recorded at 1 C for long-term cycling stability test and between 0.1 C and 5 C for rate performances based on the mass of the cathode (1 C = 148 mAh g⁻¹) between 1.0 and 2.1 V on a LAND 2001-A battery testing system at 30 °C. The corresponding EISs after 0, 15 and 100 cycles were recorded on the VMP3 electrochemical station in a frequency range of 10 mHz to 100 kHz with a disturbance amplitude of 5 mV. The Zn deposition morphology after cycling was characterized by field emission scanning electron microscope (FE-SEM, Zeiss Supra 55VP).

Material characterizations: The in-situ XRD analyses were carried out on a Bruker D8 discover diffractometer between 15 °C and 90 °C at room temperature. The electrodes were collected from the Zn||LMO cells after 25 cycles, washed with NMF and exposed to XPS depth profiling analysis. The X-ray photoelectron spectroscopy (XPS) depth profiling spectra were obtained with a PHI 5000 VersaProbe II spectrometer using a monochromatic Al Kα X-ray source at 1486.6 eV. The amount of Mn ions dissolved in the electrolyte after cycling was determined by inductively coupled plasma mass spectroscopy (ICP-MS). The cells were disassembled after 25 cycles, and the Mn ions were eluted from the glass fiber separators via a sample digestion/extraction technique in a mixed acid (4HNO₃-1HCl).

Numerical simulation: Molecular dynamics (MD) simulations were performed using NAMD.^[52] The different electrolyte systems were setup initially by using PACKMOL.^[53] Periodic boxes of 20 Å were used. The properties of H₂O are assessed with SPC/E parameters. The force-fields parameters and partial charges of Zn²⁺, Li⁺ and OTf⁻ were obtained from previous reports.^[54–58] A Lennard-Jones

(LJ) cut-off of 10 Å and a particle-particle particle-mesh solver for long-range Coulombic interactions were also employed. Velocity-Verlet algorithm was applied to integrate the equations of motion with a time step equalled to 0.5 fs. First, Langevin dynamics was performed at 500 K for 5 ns, and then NPT runs were performed at 298 K for 10 ns to ensure that the equilibrium salt dissociation had been reached. Then, the NVT runs were 20 ns long at 298 K. VMD was employed to visualize the last 1 ns trajectory, which was used to obtain the structure of the electrolyte.^[59] The hydrogen bonds were calculated considering a distance cut-off of 3.5 Å and an angle cut-off of 30°. The geometric solvation structures (Li⁺[solvent]_x[anion] or Zn²⁺[solvent]_x[anion]) were optimized at the PBE0 level (density functional theory model) with the Valence triple-zeta polarization basis sets (DEF2-TZVP) implemented into Gaussian09 package. To achieve desired structural properties, all the electrolyte systems (7.7 m LiOTf + 1 m Zn(OTf)₂ in H₂O and 7.7 m LiOTf + 1 m Zn(OTf)₂ in H₂O:NMF = 1:9) were equilibrated at 300 K, 1 atm in NPT ensemble for 10 ns before the last 5-ns trajectory was carried out to calculate the averaged density. Each system was then optimized from 1000 to 300 K three times in the NVT ensemble for another 30 ns. These systems were repeatedly simulated at the same condition, and the last 5 ns trajectory was chosen for the structural analyses.

Acknowledgements

We would like to acknowledge the financial support from the Australian Research Council (ARC) through the ARC Discovery projects (DP200101249, DP210101389, DP230101579), ARC Future Fellowship (FT220100561), ARC Linkage project (LP200200926), and ARC Industry Transformation Research Hub (IH180100020).

Conflict of Interest

The authors declare no conflict of interest.

Supporting Information

Supporting Information is available from the Wiley Online Library or from the author.

Keywords

aqueous electrolytes, electrolyte solvation structures, high-voltage zinc batteries, hybrid batteries

Received: November 4, 2022

Revised: December 12, 2022

Published online: December 12, 2022

- [1] H. Zhang, X. Liu, H. Li, I. Hasa, S. Passerini, *Angew. Chem. Int. Ed.* **2021**, *60*, 598.
- [2] H. Pan, Y. Shao, P. Yan, Y. Cheng, K. S. Han, Z. Nie, C. Wang, J. Yang, X. Li, P. Bhattacharya, K. T. Mueller, J. Liu, *Nat. Energy* **2016**, *1*, 16039.
- [3] L. Droguet, A. Grimaud, O. Fontaine, J. M. Tarascon, *Adv. Energy Mater.* **2020**, *10*, 2002440.
- [4] J. Liu, W. Zhou, R. Zhao, Z. Yang, W. Li, D. Chao, S.-Z. Qiao, D. Zhao, *J. Am. Chem. Soc.* **2021**, *143*, 15475.
- [5] L. Yan, Y. Zhang, Z. Ni, Y. Zhang, J. Xu, T. Kong, J. Huang, W. Li, J. Ma, Y. Wang, *J. Am. Chem. Soc.* **2021**, *143*, 15369.
- [6] D. H. Jang, Y. J. Shin, S. M. Oh, *J. Electrochem. Soc.* **1996**, *143*, 2204.
- [7] B. Sambandam, V. Mathew, S. Kim, S. Lee, S. Kim, J. Y. Hwang, H. J. Fan, J. Kim, *Chem* **2022**, *8*, 924.
- [8] L. Suo, O. Borodin, T. Gao, M. Olguin, J. Ho, X. Fan, C. Luo, C. Wang, K. Xu, *Science* **2015**, *350*, 938.

- [9] L. Suo, O. Borodin, W. Sun, X. Fan, C. Yang, F. Wang, T. Gao, Z. Ma, M. Schroeder, A. von Cresce, S. M. Russell, M. Armand, A. Angell, K. Xu, C. Wang, *Angew. Chem. Int. Ed.* **2016**, *55*, 7136.
- [10] L. Chen, J. Zhang, Q. Li, J. Vatamanu, X. Ji, T. Pollard, A. Cui, S. Hou, J. Chen, C. Yang, L. Ma, M. Ding, M. N. Garaga, S. Greenbaum, H.-S. Lee, O. Borodin, K. Xu, C. Wang, *ACS Energy Lett.* **2020**, *5*, 968.
- [11] X. Song, H. He, M. H. A. Shiraz, H. Zhu, A. Khosrozadeh, J. Liu, *Chem. Commun.* **2021**, *57*, 1246.
- [12] Y. Yang, S. Liang, B. Lu, J. Zhou, *Energy Environ. Sci.* **2022**, *15*, 1192.
- [13] J. Zhao, J. Zhang, W. Yang, B. Chen, Z. Zhao, H. Qiu, S. Dong, X. Zhou, G. Cui, L. Chen, *Nano Energy* **2019**, *57*, 625.
- [14] X. He, B. Yan, X. Zhang, Z. Liu, D. Bresser, J. Wang, R. Wang, X. Cao, Y. Su, H. Jia, *Nat. Commun.* **2018**, *9*, <https://doi.org/10.1038/s41467-018-07331-6>.
- [15] P. Jaumaux, X. Yang, B. Zhang, J. Safaei, X. Tang, D. Zhou, C. Wang, G. Wang, *Angew. Chem. Int. Ed.* **2021**, *60*, 19965.
- [16] J. Xie, Z. Liang, Y.-C. Lu, *Nat. Mater.* **2020**, *19*, 1006.
- [17] X. Qiu, N. Wang, X. Dong, J. Xu, K. Zhou, W. Li, Y. Wang, *Angew. Chem. Int. Ed.* **2021**, *60*, 21025.
- [18] A. Naveed, H. Yang, J. Yang, Y. Nuli, J. Wang, *Angew. Chem. Int. Ed.* **2019**, *58*, 2760.
- [19] A. Naveed, H. Yang, Y. Shao, J. Yang, N. Yanna, J. Liu, S. Shi, L. Zhang, A. Ye, B. He, *Adv. Mater.* **2019**, *31*, 1900668.
- [20] X. Ma, X. Cao, M. Yao, L. Shan, X. Shi, G. Fang, A. Pan, B. Lu, J. Zhou, S. Liang, *Adv. Mater.* **2022**, *34*, 2105452.
- [21] Y. Ma, Q. Zhang, L. Liu, Y. Li, H. Li, Z. Yan, J. Chen, *Natl. Sci. Rev.* **2022**, *9*, nwac051.
- [22] A. Dey, F. E. Jenney, M. W. Adams, E. Babini, Y. Takahashi, K. Fukuyama, K. O. Hodgson, B. Hedman, E. I. Solomon, *Science* **2007**, *318*, 1464.
- [23] A. Miura, N. C. Rosero-Navarro, A. Sakuda, K. Tadanaga, N. H. Phuc, A. Matsuda, N. Machida, A. Hayashi, M. Tatsumisago, *Nat. Rev. Chem.* **2019**, *3*, 189.
- [24] J. Shi, T. Sun, J. Bao, S. Zheng, H. Du, L. Li, X. Yuan, T. Ma, Z. Tao, *Adv. Funct. Mater.* **2021**, *31*, 2102035.
- [25] K. Fujii, H. Wakamatsu, Y. Todorov, N. Yoshimoto, M. Morita, *J. Phys. Chem. C* **2016**, *120*, 17196.
- [26] X. Wu, Y. Xu, C. Zhang, D. P. Leonard, A. Markir, J. Lu, X. Ji, *J. Am. Chem. Soc.* **2019**, *141*, 6338.
- [27] G. Maisano, P. Migliardo, M. P. Fontana, M. C. Bellissent-Funel, A. J. Dianoux, *J. Phys. C Solid State Phys.* **1985**, *18*, 1115.
- [28] Y. Wang, M. Guo, S. Wei, S. Yin, Y. Wang, Z. Song, M. R. Hoffmann, *Comput. Theor. Chem.* **2014**, *1049*, 28.
- [29] T. Forsting, H. C. Gottschalk, B. Hartwig, M. Mons, M. A. Suhm, *Phys. Chem. Chem. Phys.* **2017**, *19*, 10727.
- [30] Y. Dong, S. Di, F. Zhang, X. Bian, Y. Wang, J. Xu, L. Wang, F. Cheng, N. Zhang, *J. Mater. Chem. A* **2020**, *8*, 3252.
- [31] S.-I. Nakano, Y. Kitagawa, D. Miyoshi, N. Sugimoto, *FEBS Open Bio* **2014**, *4*, 643.
- [32] Y. Zhang, G. Wan, N. H. C. Lewis, J. Mars, S. E. Bone, H.-G. Steinrück, M. R. Lukatskaya, N. J. Weadock, M. Bajdich, O. Borodin, A. Tokmakoff, M. F. Toney, E. J. Maginn, *ACS Energy Lett.* **2021**, *6*, 3458.
- [33] T. C. Li, Y. Lim, X. L. Li, S. Luo, C. Lin, D. Fang, S. Xia, Y. Wang, H. Y. Yang, *Adv. Energy Mater.* **2022**, *12*, 2103231.
- [34] X. Ren, S. Chen, H. Lee, D. Mei, M. H. Engelhard, S. D. Burton, W. Zhao, J. Zheng, Q. Li, M. S. Ding, M. Schroeder, J. Alvarado, K. Xu, S. Y. Meng, J. Liu, J.-G. Zhang, W. Xu, *Chem* **2018**, *4*, 1877.
- [35] Z. Hou, L. Zhang, J. Chen, Y. Xiong, X. Zhang, Y. Qian, *Mater. Chem. Front.* **2021**, *5*, 2749.
- [36] R. Tian, S.-H. Park, P. J. King, G. Cunningham, J. Coelho, V. Nicolosi, J. N. Coleman, *Nat. Commun.* **2019**, *10*, 1933.
- [37] T. Joshi, K. Eom, G. Yushin, T. F. Fuller, *J. Electrochem. Soc.* **2014**, *161*, A1915.
- [38] M. B. Pinson, M. Z. Bazant, *J. Electrochem. Soc.* **2012**, *160*, A243.
- [39] P. T. Gilbert, *J. Electrochem. Soc.* **1952**, *99*, 16.
- [40] W. Sun, F. Wang, S. Hou, C. Yang, X. Fan, Z. Ma, T. Gao, F. Han, R. Hu, M. Zhu, C. Wang, *J. Am. Chem. Soc.* **2017**, *139*, 9775.
- [41] S. Xie, Y. Li, L. Dong, *J. Energy Chem.* **2023**, *76*, 32.
- [42] B. Li, X. Zhang, T. Wang, Z. He, B. Lu, S. Liang, J. Zhou, *Nanomicro Lett.* **2021**, *14*, 6.
- [43] J. Shin, J. Lee, Y. Park, J. W. Choi, *Chem. Sci.* **2020**, *11*, 2028.
- [44] D. Li, L. Cao, T. Deng, S. Liu, C. Wang, *Angew. Chem. Int. Ed.* **2021**, *60*, 13035.
- [45] S. Di, X. Nie, G. Ma, W. Yuan, Y. Wang, Y. Liu, S. Shen, N. Zhang, *Energy Stor. Mater.* **2021**, *43*, 375.
- [46] C. Huang, X. Zhao, S. Liu, Y. Hao, Q. Tang, A. Hu, Z. Liu, X. Chen, *Adv. Mater.* **2021**, *33*, 2100445.
- [47] S. Zhao, Z. Liu, G. Xie, X. Guo, Z. Guo, F. Song, G. Li, C. Chen, X. Xie, N. Zhang, B. Sun, S. Guo, G. Wang, *Angew. Chem. Int. Ed.* **2021**, *60*, 26246.
- [48] D. Weng, H. Duan, Y. Hou, J. Huo, L. Chen, F. Zhang, J. Wang, *Prog. Nat. Sci.* **2020**, *30*, 139.
- [49] M. A. Kamenskii, S. N. Eliseeva, A. I. Volkov, V. V. Kondratiev, *J. Electrochem. Sci. Technol.* **2022**, *13*, 177.
- [50] T. Liu, A. Dai, J. Lu, Y. Yuan, Y. Xiao, L. Yu, M. Li, J. Gim, L. Ma, J. Liu, *Nat. Commun.* **2019**, *10*, 1.
- [51] P. Jaumaux, Q. Liu, D. Zhou, X. Xu, T. Wang, Y. Wang, F. Kang, B. Li, G. Wang, *Angew. Chem. Int. Ed.* **2020**, *59*, 9134.
- [52] J. C. Phillips, D. J. Hardy, J. D. Maia, J. E. Stone, J. V. Ribeiro, R. C. Bernardi, R. Buch, G. Fiorin, J. Hénin, W. Jiang, *J. Chem. Phys.* **2020**, *153*, 044130.
- [53] L. Martínez, R. Andrade, E. G. Birgin, J. M. Martínez, *J. Comput. Chem.* **2009**, *30*, 2157.
- [54] T. Mendez-Morales, Z. Li, M. Salanne, *Batter. Supercaps* **2021**, *4*, 646.
- [55] A. Pérez de la Luz, J. A. Aguilar-Pineda, J. G. Méndez-Bermúdez, J. Alejandro, *J. Chem. Theory Comput.* **2018**, *14*, 5949.
- [56] S. Obst, H. Bradaczek, *J. Mol. Model.* **1997**, *3*, 224.
- [57] A. P. Sunda, A. Venkatnathan, *J. Comput. Chem.* **2011**, *32*, 3319.
- [58] I. Skarmoutsos, J. Samios, *Chem. Phys. Lett.* **2004**, *384*, 108.
- [59] W. Humphrey, A. Dalke, K. Schulten, *J. Mol. Graph.* **1996**, *14*, 33.